ISA Transactions 139 (2023) 436–447

Contents lists available at ScienceDirect

ISA Transactions

journal homepage: www.elsevier.com/locate/isatrans

Practice article

Sliding-mode anti-disturbance speed control of permanent magnet synchronous motor based on an advanced reaching law

Ying Qu [a,b], Bin Zhang [a], Hairong Chu [a,*], Honghai Shen [a], Jingzhong Zhang [c], Xiaoxia Yang [a]

[a] Changchun Institute of Optics, Fine Mechanics, and Physics, Chinese Academy of Science, Changchun 130033, China
[b] The University of Chinese Academy of Sciences, Beijing 100049, China
[c] Forest Protection Research Institute of Heilongjiang, Harbin 150040, China

ARTICLE INFO

Article history:
Received 20 August 2022
Received in revised form 31 March 2023
Accepted 14 April 2023
Available online 25 April 2023

Keywords:
Sliding mode control (SMC)
Advanced sliding mode reaching law (ASMRL)
Sliding mode disturbance observer (SMDO)
Permanent magnet synchronous motor (PMSM)

ABSTRACT

In order to improve the performance of a permanent magnet synchronous motor (PMSM) speed controller, an advanced reaching law sliding mode control (ASMC) strategy is proposed in this study. The advanced sliding mode reaching law (ASMRL) introduces a power term of the system state and a checkmark function term about the sliding mode function based on the traditional constant-proportional rate reaching law(TSMRL) , and replaces the sign function with a hyperbolic tangent function. A detailed theoretical analysis of the characteristics of the ASMRL is then presented. The theoretical analysis shows that the ASMRL converges to the sliding mode surface more quickly and with less chattering than the TSMRL. In addition, a sliding mode disturbance observer (SMDO) is designed to estimate the total disturbance of the system, and the estimated disturbance is compensated to ASMC. Then the stability of the system with ASMC and the stability of the system with ASMC+SMDO is proved by Lyapunov's theorem. Finally, the proposed control strategy is validated on an experimental platform of PMSM. The experimental results show that the ASMC has a faster convergence speed, smaller chattering, better disturbance rejection performance than the traditional constant-proportional rate reaching law sliding mode control(TSMC), and better performance with the addition of SMDO.

1. Introduction

PMSMs are increasingly widely used in many modern alternating current servo systems such as robotics, electric vehicles, computerized numerical control (CNC) machine tools, and aerospace due to their high performance, high power density, simple structure, and light weight [1]. The most classical control strategy is proportional–integral (PI) control, which is widely used in linear constant systems because of its advantages such as simple structure and good stability [2]. However, the PMSM is a multivariable strongly coupled nonlinear system [3]. In practical application, PMSM is affected by various disturbances, such as external load disturbance and internal parameter mismatch, etc. [4], all these factors make it difficult to achieve higher control performance with the PI control strategy.

To overcome the influence of various disturbances mentioned above and to improve the performance of control strategies, more and more high-performance and high-precision control strategies have been proposed in recent years. Such as fuzzy control [5,6], model predictive control [7,8], active disturbance rejection control [9,10], neural network control [11–13], sliding mode control (SMC) [14,15], etc. Among them, SMC has attracted high attention in the control field because of its simple structure, low requirements for model accuracy, and insensitivity to perturbations [16]. At present, SMC has been successfully applied to motor speed control systems [17]. However, sliding modes have inherent chattering problems, and Arie Levant classified sliding mode chattering and also studied the effect of each type of chattering on control [18]. In conventional sliding mode control, chattering caused by the discontinuity of the system and the switching term in the sliding mode reaching law is very detrimental to the control process [19]. Therefore, the chattering phenomenon is one of the important problems to be solved in SMC.

In order to solve the chattering of SMC and to improve the performance of SMC, scholars have continued to deepen the research on SMC. Various forms of SMC have been proposed, such as high-order SMC [20], fast terminal SMC [21], and non-singular terminal SMC [22]. There are also studies that combine SMC with other control algorithms to improve the control performance of SMC. In [23], Sami et al. combined fuzzy control with fractional-order terminal SMC to solve the inherent chattering problem and maintain the robustness and stability of the system. Fei et al. proposed an adaptive SMC system using a two-loop recurrent neural network structure [24]. This method can achieve good tracking

* Corresponding author.
E-mail address: chuhr@ciomp.ac.cn (H. Chu).

https://doi.org/10.1016/j.isatra.2023.04.016
0019-0578/

performance and can estimate the unknown disturbances quickly and accurately. However, in the actual control process, the system is affected by various internal and external disturbances. In order to attenuate the effects of these disturbances on the system, the SMDO is proposed. In recent years, the SMDO and various composite control strategies combined with the SMDO have been intensively studied. Guo et al. proposed an improved SMDO in [25]. The low-pass filter of the conventional SMDO is replaced with an adaptive complex coefficient filter. Also, a nonlinear saturation function is used instead of the sign function to reduce the chattering of the SMDO. This method can improve the speed and position observation accuracy of the SMDO. Wang et al. proposed a speed adaptive flux SMDO [26]. A transition mode is introduced between the reaching mode and sliding mode of this observer, and an algorithm based on the error criterion function is designed to adjust the sliding mode gain online. In addition, a new speed adaptive law is proposed based on the model reference adaptive system and the speed adaptive flux SMDO. Yan et al. proposed a sliding mode observer to estimate the system state and an adaptive law to estimate the unknown parameters. Simulations of the bioreactor system showed the effectiveness of the method [27].

An overview of the research on SMC reveals that the inherent chattering of SMC is fundamentally due to the switching term in the reaching law [28]. Therefore, in addition to the above-mentioned methods to improve chattering, a fundamental approach to improve the reaching law is also an effective way to solve sliding mode chattering. Mozayan et al. proposed a control scheme for a variable speed direct drive wind energy conversion system (WECS) based on sliding mode control (SMC) for grid-connected permanent magnet synchronous generators. This control strategy modifies the reaching law (RL) of the sliding mode technique to reduce the chattering problem and improve the total harmonic distortion performance compared to the conventional RL SMC [29]. Leśniewski et al. introduced a new non-switching reaching law for sliding mode control of discrete-time systems. These improvements were obtained by applying a modified definition of quasi-sliding mode and introducing a tunable, state-dependent sliding variable descent rate factor was obtained [30]. In [31], Wang et al. proposed an SMC method based on a new sliding mode reaching law. This new reaching law includes the system state variables and a power term of the sliding surface function that is bounded by the absolute value of the switching function. In addition, an extended state observer is introduced to centrally observe the disturbances. Experimental results show that the method not only reduces chattering but also improves the speed of the system state reaching the sliding mode surface. Junejo et al. proposed a new adaptive terminal sliding mode reaching law and continuous fast terminal sliding mode control [32]. Secondly, an extended SMDO is designed to estimate the total disturbance of the system to improve the disturbance rejection of the system. The proposed adaptive terminal sliding mode reaching law can improve the arrival speed under startup and load transients and can effectively suppress the chattering phenomenon.

Consequently, an ASMRL is proposed in this paper. The ASMRL introduces a power term concerning the system state and a checkmark function term concerning the sliding mode function, and replaces the sign function with a hyperbolic tangent function to further reduce chattering. The ASMRL has a faster convergence rate and less chattering than the TSMRL. In addition, to further enhance the robustness of the system, an SMDO is designed to estimate and compensate for the total disturbance of the system. Regarding the system stability of the ASMC and ASMC+SMDO control strategies proposed in this paper, it is also proved using Lyapunov's theorem. The main contributions of this paper are as follows.

(1) An ASMRL is proposed to reduce the arrival time while also reducing chattering.

(2) An SMDO is designed to observe and compensate for the total disturbance of the system, which improves the robustness of the system.

(3) Several sets of experiments are designed to verify that the proposed sliding mode anti-disturbance controller based on the ASMRL has better dynamic and steady-state characteristics.

The rest of this paper is organized as follows. Section 2 gives the mathematical model of PMSM. Section 3 gives the expressions of the ASMRL with its characteristics in detail. Then the discrete form of the ASMRL is given, and the performance of several different forms of reaching laws is compared. In Section 4, a sliding mode controller based on the ASMRL and an SMDO are designed. And the system stabilities of ASMC and ASMC+SMDO control strategies are proved. Section 5 compares and analyzes the experimental results of PI, TSMC, RSMC, ASMC, and ASMC+SMDO control strategies on the PMSM experimental platform. Conclusions are drawn in Section 6.

2. Mathematical model of a PMSM

Assuming symmetrical windings and neglecting core saturation and disregarding eddy current losses and hysteresis losses, the mathematical model of a PMSM can be obtained according to the motor control theory in [33].

The stator voltage equations in the d-q synchronous rotating coordinate system are given as follows:

$$U_d = Ri_d + \frac{d\psi_d}{dt} - \omega_e \psi_q \tag{1}$$

$$U_q = Ri_q + \frac{d\psi_q}{dt} + \omega_e \psi_d \tag{2}$$

where U_q, U_d, i_q, and i_d are the stator voltage and current in the d-q coordinate system, respectively. ω_e is the electric angular velocity, and R is the stator resistance. $\psi_d = L_d i_d + \psi_f$ and $\psi_q = L_q i_q$ are the stator flux linkages in the d-q coordinate system, where L_d and L_q are the inductances in the d-q coordinate system and ψ_f is the flux amplitude of the permanent magnet.

The electromagnetic torque equation is expressed as follows:

$$T_e = \frac{3}{2} n_p \left(\psi_d i_q - \psi_q i_d\right) \tag{3}$$

where T_e is the electromagnetic torque and n_p is the number of pole pairs.

The motion equation is as follows:

$$J\frac{d\omega_m}{dt} = T_e - T_L - B\omega_m \tag{4}$$

where J is the moment of inertia, ω_m is the mechanical angular velocity, T_L is the load torque, and B is the viscous friction coefficient.

3. Sliding mode control based on an advanced reaching law

3.1. SMC design with TSMRL

SMC is a special type of variable structure control, which is essentially a nonlinear control. The following second-order system is used as an example to design the SMC [34].

$$\begin{cases} x_1 = \dot{x}_2 \\ \dot{x}_2 = -f(x) + d(x,t) + bu(t) \end{cases} \tag{5}$$

where x_1, x_2 is a system state variable, b is a constant, and $b \neq 0$, $f(x)$ is a continuous function, $d(x,t)$ is the total system perturbation, and $d(x,t)$ is bounded.

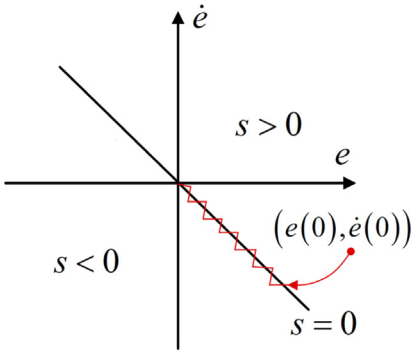

Fig. 1. Schematic diagram of the sliding mode motion process.

The design of the SMC is divided into two steps, first a sliding mode function is designed as follows :

$$s = cx_1 + x_2 \tag{6}$$

where c is a constant that satisfies the Hurwitz condition.

The second step is to design the sliding mode reaching law. The TSMRL was first proposed by Gao [35], as shown in (7).

$$\dot{s} = -\varepsilon \mathrm{sgn}(s) - ks \tag{7}$$

where ε and k are parameters to be determined, and $\varepsilon > 0, k > 0$.

According to (5)–(7), the controller is designed as:

$$u(t) = \frac{1}{b}\left[-c\dot{x}_1 + f(x) - d(x,t) - ks - \varepsilon \mathrm{sgn}(s)\right] \tag{8}$$

3.2. Characteristic analysis of TSMRL

The control characteristics of SMC can force the system state to move along a sliding mode, which is designable and independent of the system parameters and perturbations. Therefore, once the system state trajectory reaches the sliding mode surface, the system has strong robustness. The motion of the system state trajectory is divided into two processes, reaching motion and sliding mode motion, as shown in Fig. 1. After the system trajectory enters the sliding mode motion process, its motion trajectory will make small amplitude and high frequency motion along the sliding mode surface $s = 0$. Therefore, the design of the reaching law directly affects the trajectory of the system state.

In the TSMRL (7), $-\varepsilon \mathrm{sgn}(s)$ is the constant rate reaching term and $-ks$ is the proportional rate reaching term. The proportional rate reaching term $-ks$ ensures that the system state can converge to the sliding mode surface with a large velocity when s is large. However, with only the proportional rate term, the velocity of the moving point approaching the sliding mode surface becomes smaller and smaller as it approaches the sliding mode surface, which is an asymptotic process and cannot guarantee a finite time arrival, so the constant rate reaching term $-\varepsilon \mathrm{sgn}(s)$ is introduced. The constant rate reaching term can guarantee that the approaching velocity is ε instead of zero when the moving point reaches the sliding mode surface, i.e., it can guarantee a finite time arrival. When ε is small, the approaching velocity is slow, and when ε is large, then the moving point arrives at the sliding mode surface with a large velocity, which will cause a large chattering phenomenon. In summary, it can be seen that the faster the system state reaches the sliding mode surface, the larger the chattering will be caused, so in order to solve the conflict between the sliding mode approaching speed and chattering, the design of an effective new reaching law is a feasible and effective solution.

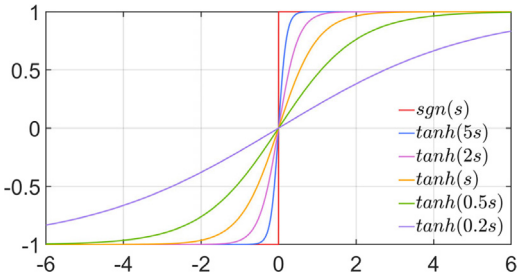

Fig. 2. Images of $\tanh(\lambda s)$ and $sgn(s)$.

3.3. Design and analysis of the ASMRL

In this paper, based on the TSMRL and reference sliding mode reaching law (RSMRL) in [31], an adavanced reaching law in the form of (9) is proposed.

$$\dot{s} = -\varepsilon |x|^a \tanh(\lambda s) - ks\left(\alpha_1 |s|^b + \frac{\alpha_2}{|s|^b}\right) \tag{9}$$

where x denotes the system state and $\lim_{t\to\infty} |x| = 0$. ε, k, a, b, α_1, α_2 are parameters to be determined, and $\varepsilon > 0, k > 0, 1 > a > 0$, $1 > b > 0, \alpha_1 > \alpha_2 > 0$.

In the constant rate reaching term, an power term about the system state $|x|^a$ is introduced, so that the constant rate reaching term decreases gradually from a large value in the process of the system state from far away from the sliding mode surface to reaching the sliding mode surface, which ensures a reasonable change of the approaching speed and reduces the chattering. In addition, the sign function $sgn(s)$ is replaced by the hyperbolic tangent function $\tanh(\lambda s)$ to further reduce the chattering. The expression of $\tanh(\lambda s)$ is shown in (10), and the images of function $\tanh(\lambda s)$ and $sgn(s)$ are shown in Fig. 2. It can be seen that the smaller the parameter λ is, the smoother the isokinetic reaching term is in the process of convergence to zero, and the smaller the chattering is.

$$\tanh(\lambda s) = \frac{e^{\lambda s} - e^{-\lambda s}}{e^{\lambda s} + e^{-\lambda s}} \tag{10}$$

In the proportional rate reaching term, a checkmark function $\alpha_1|s|^b + \frac{\alpha_2}{|s|^b}$ is introduced and its image is shown in Fig. 3. In the figure, $y = \alpha_1|s|^b$ and $y = \frac{\alpha_2}{|s|^b}$ are the two asymptotes of the checkmark function, respectively. The two extreme points of the checkmark function are $\left(-\sqrt[2b]{\frac{\alpha_2}{\alpha_1}}, 2\sqrt{\alpha_1\alpha_2}\right)$, $\left(\sqrt[2b]{\frac{\alpha_2}{\alpha_1}}, 2\sqrt{\alpha_1\alpha_2}\right)$, respectively. The proportional rate reaching term with the checkmark function has the following characteristics. Taking the extreme point as the dividing point, when the system state is far away from the sliding mode surface, i.e., $|s| > \sqrt[2b]{\frac{\alpha_2}{\alpha_1}}$, the coefficient of the proportional rate term increases with the increase of s. In other words, the farther the system state is from the sliding mode surface, the faster the approaching speed can be. When the system state gradually approaches the sliding mode surface to $|s| < \sqrt[2b]{\frac{\alpha_2}{\alpha_1}} < 1$, and then reaches the sliding mode surface $s = 0$, the traditional constant rate term $-ks$ will gradually converge to 0 in this process. And the closer to the sliding mode surface, the smaller the approaching speed. While in the case of $|s| < \sqrt[2b]{\frac{\alpha_2}{\alpha_1}} < 1$, the checkmark function is increasing as $|s|$ decreases, so the checkmark function improves the approaching speed of this process, making the approaching speed of this phase faster than TSMRL.

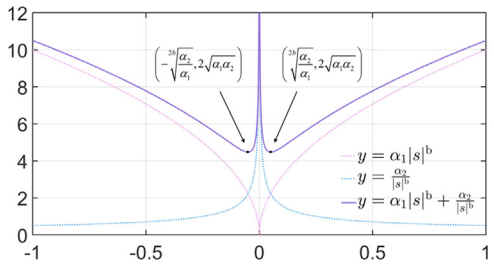

Fig. 3. Checkmark function and its asymptotes.

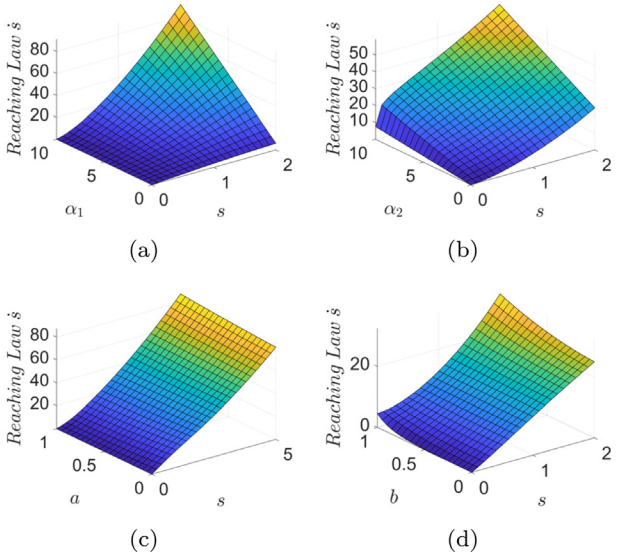

Fig. 4. Influence of different parameter variation on the reaching law when the system sliding mode is approached from far to near. (a) Three-dimensional diagram of the effect of parameter α_1. (b) Three-dimensional diagram of the effect of parameter α_2. (c) Three-dimensional diagram of the effect of parameter a. (d) Three-dimensional diagram of the effect of parameter b.

In order to analyze more intuitively the influence of each parameter on the newly proposed advanced reaching law, the three-dimensional diagrams shown in Fig. 4 are given. Fig. 4 shows that α_1 mainly affects the reaching law when the system state is far from the sliding mode surface. The larger α_1 is and the farther the system state is from the sliding mode surface, the larger the reaching law is. In addition, the increase of α_1 hardly affects the reaching law when the system state reaches the sliding mode surface, i.e., the increase of α_1 does not increase the chattering. α_2 also increases the reaching law, but unlike α_1, with the increase of α_2, the reaching law when the system state reaches the sliding mode surface also increases, i.e., the larger α_2 is, the larger the chattering will be. a has a weaker effect on the reaching law. With the increase of a, the reaching law of the system state at the same position increases weakly. The increase of b will increase the reaching law when the system state is far away from the sliding mode surface and arrives at the sliding mode surface, i.e., the increase of b will speed up the reaching speed, but it also tends to cause chattering. In summary, a and α_1 can be taken as larger values in their respective ranges, but b and α_2 are preferred to be taken as smaller values in their respective ranges to avoid aggravating chattering.

3.4. Discrete form of the ASMRL

In practical engineering applications, the implementation of control algorithms is in discrete form. So in this section, the discrete form of the ASMRL is analyzed. If the sliding mode function s converges to 0, Eq. (9) can be approximated as Eq. (11).

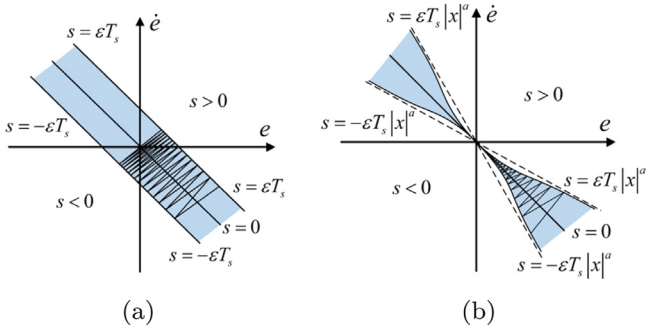

Fig. 5. Comparison of system state trajectories. (a) TSMRL (b) ASMRL.

$$\dot{s} \approx -\varepsilon|x|^a \tanh(\lambda s) \tag{11}$$

Its discrete form can be expressed as

$$s(n+1) - s(n) = -\varepsilon T_s|x|^a \tanh(\lambda s(n)) \tag{12}$$

where T_s is the sampling time.

Assume that the system trajectory can reach the sliding mode surface from $s > 0$ in finite step, which indicates that $s(n) = 0^+$. Also combining with Eq. (10) and Fig. 2, we have $|\tanh(\lambda s)| < |\mathrm{sgn}(s)|$, that is, $sgn(s)$ can be regarded as the boundary of $\tanh(\lambda s)$. It can be derived that $\tanh(\lambda s) < \mathrm{sgn}(s)$ when $s > 0$. Then, using the inequality scaling method, the following equation can be obtained in the next period.

$$s(n+1) > -\varepsilon T_s|x|^a \tag{13}$$

Similarly, assume that the system trajectory can reach the sliding mode surface from $s < 0$ in finite step, which shows that $s(n) = 0^-$. At $s < 0$ it can be derived that $\tanh(\lambda s) > \mathrm{sgn}(s)$. Then, using the inequality scaling method, the following equation can be obtained in the next period.

$$s(n+1) < \varepsilon T_s|x|^a \tag{14}$$

Combining (13) and (14), it can be deduced that the width of the discrete sliding mode band Δ satisfies

$$\Delta < 2\varepsilon T_s|x|^a \tag{15}$$

The discrete form of the TSMRL (7) is

$$s_0(n+1) - s_0(n) = -\varepsilon_0 T_s \mathrm{sgn}(s_0(n)) \tag{16}$$

The width of its discrete sliding mode band Δ_0 is

$$\Delta_0 = 2\varepsilon T_s \tag{17}$$

Comparing (14) and (17), it can be seen that the bandwidth of the sliding mode band of the TSMRL is a constant, which causes the system to fail to reach the equilibrium state, and the system state will generate chattering between $-\varepsilon T_s$ and εT_s. In contrast, the bandwidth of the sliding mode band of the ASMRL is a variable quantity that varies with the system state, and the system state will converge to an equilibrium point, as shown in Fig. 5.

3.5. Performance comparison of several reaching laws

To compare the performance of the TSMRL, RSMRL, and ASMRL, the classical motor model shown in (18) is established [34].

$$\ddot{\theta}(t) = -f(\theta, t) + b_0 u(t) + d(t) \tag{18}$$

where $f(\theta, t) = 25\dot{\theta}$ is the position signal, $u(t)$ is the control input, $b_0 = 133$ is a constant, and $d(t)$ is the lumped disturbance. The sliding mode surface is chosen in the following form.

$$s(t) = ce(t) + \dot{e}(t) \tag{19}$$

where c is a positive constant that satisfies the Hurwitz condition. The error $e(t) = \theta_d(t) - \theta(t)$, and $\theta_d(t)$ is the reference position signal.

Combining (9), (18), and (19), the control input can be derived as follows.

$$\begin{aligned} u(t) = &\frac{1}{b_0}\left[c\left(\dot{\theta}_{\mathrm{d}} - \dot{\theta}\right) + \ddot{\theta}_{\mathrm{d}} + f(\theta, t) - d(t)\right. \\ &\left. + \varepsilon|x|^a \tanh(\lambda s) + ks\left(\alpha_1|s|^{\mathrm{b}} + \frac{\alpha_2}{|s|^{\mathrm{b}}}\right)\right] \end{aligned} \tag{20}$$

The parameters are set as follows, $c = 5$, $k = 25$, $\varepsilon = 5$, $\lambda = 1$, $a = 0.5$, $b = 0.3$, $\alpha_1 = 10$, $\alpha_2 = 0.1$, the reference position signal is set as $\theta_d(t) = sin(t)$, the lumped disturbance is set as $d(t) = 10\sin(\pi t)$, and the initial system state is set as $[x_1, x_2] = [-2, -2]$, x_1 and x_2 are the state variables of the system.

Fig. 6 compares the performance of TSMRL, RSMRL, and ASMRL. Fig. 6(a) shows the phase trajectory of the system state from the initial position to the sliding mode surface with the three reaching laws. It can be seen that ASMRL has a faster convergence rate than TSMRL and RSMRL. Fig. 6(b) illustrates the control inputs with the three reaching laws, which shows that ASMRL has smoother control inputs with minimum chattering than TSMRL and RSMRL. Fig. 6(c) shows the position tracking curves with the three reaching laws, showing that ASMRL is the fastest to keep up with the reference position signal. Fig. 6(d) and Fig. 6(e) present the convergence process of the system state with the three reaching laws, as seen that ASMRL has a smaller steady state error compared to TSMRL and RSMRL. In summary, ASMRL has superior performance in terms of convergence speed, steady state error, and chattering suppression.

4. Design of speed controller based on the ASMRL

4.1. Design of the advanced reaching law sliding mode speed controller

According to the mathematical model of PMSM (1)–(4), the speed control object of the motor can be deduced as a first-order system of the following form.

$$\begin{aligned} \dot{\omega}_m &= \frac{3n_p\psi_f}{2J}i_q - \frac{1}{J}T_L - \frac{B}{J}\omega_m \\ &= \alpha i_q - \beta T_L - \gamma\omega_m \end{aligned} \tag{21}$$

Where, $\alpha = \frac{3n_p\psi_f}{2J}$, $\beta = \frac{1}{J}$, $\gamma = \frac{B}{J}$. When considering the case of parameter mismatch, (21) is rewritten as

$$\begin{aligned} \dot{\omega}_m &= \frac{3n_p\left(\psi_f + \Delta\psi_f\right)}{2(J + \Delta J)}i_q - \frac{1}{(J + \Delta J)}T_L - \frac{(B + \Delta B)}{(J + \Delta J)}\omega_m \\ &= (\alpha + \Delta\alpha)i_q - (\beta + \Delta\beta)T_L - (\gamma + \Delta\gamma)\omega_m \end{aligned} \tag{22}$$

where $\Delta\alpha = \frac{3n_p(\Delta\psi_f J - \psi_f \Delta J)}{2J(J+\Delta J)}$, $\Delta\beta = \frac{-\Delta J}{J(J+\Delta J)}$, and $\Delta\gamma = \frac{J\Delta B - B\Delta J}{J(J+\Delta J)}$ are the corresponding parameter mismatch terms.

The total system perturbation is defined as $d(t)$, which consists of the internal parameter perturbation and the external load perturbation of the system. Its expression is as follows.

$$d(t) = \Delta\alpha i_q - (\beta + \Delta\beta)T_L - \Delta\gamma\omega_m \tag{23}$$

And assume that the total system perturbation satisfies

$$|d(t)| \le d_0 \tag{24}$$

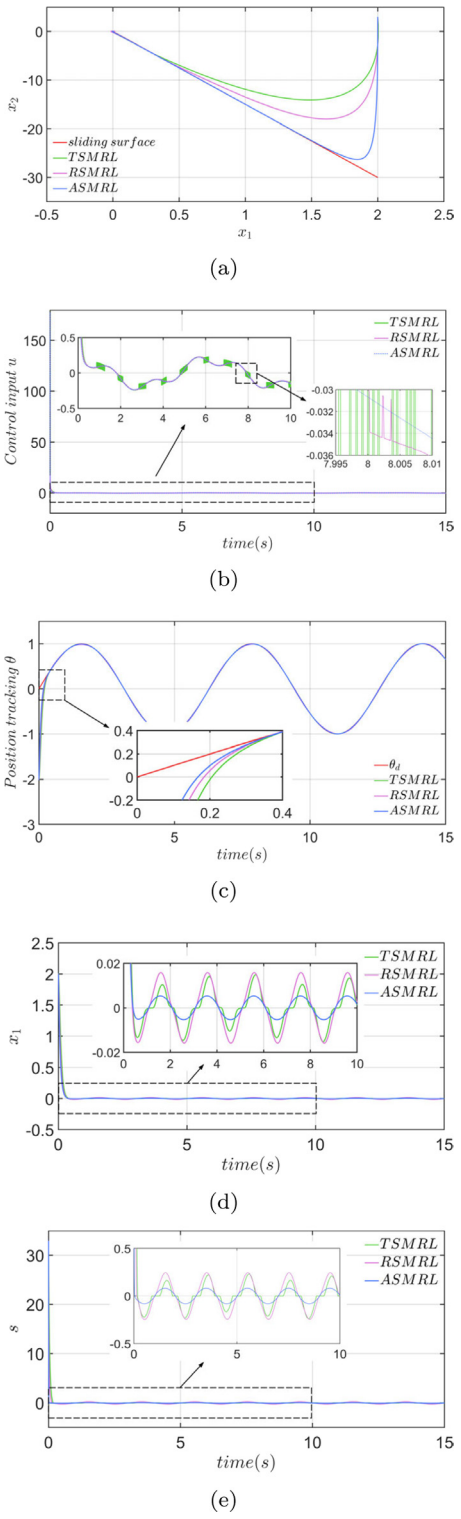

Fig. 6. Performance comparison between TSMRL, RSMRL, and ASMRL. (a) Phase trajectory (b) Control input (c) Position tracking (d) System state convergence process (e) Sliding mode convergence process.

where d_0 is the upper bound of the system perturbation. So Eq. (22) can be rewritten as

$$\dot{\omega}_m = \alpha i_q - \gamma\omega_m + d(t) \tag{25}$$

The speed error is defined as

$$e = \omega_{ref} - \omega_m \tag{26}$$

where ω_{ref} is the speed reference value and ω_m is the actual speed feedback value. In this paper, the integral type sliding surface is chosen in the following form.

$$s = e + c\int_0^t edt \tag{27}$$

The derivative of the sliding mode surface is

$$\dot{s} = \dot{e} + ce \tag{28}$$

Using the advanced reaching law (9) proposed in this paper, combined with (25)–(28), the current reference value i_{qref}, i.e., the speed control input, can be deduced as

$$\begin{aligned} u(t) = \frac{1}{b}\Big[&\dot{\omega}_{ref} + c\omega_m - d(t) + ce \\ &+\varepsilon|x|^a \tanh(\lambda s) + ks\left(\alpha_1|s|^{\mathrm{b}} + \frac{\alpha_2}{|s|^{\mathrm{b}}}\right)\Big] \end{aligned} \tag{29}$$

From (29), it can be seen that the total disturbance of the system is feedback to the control law as a known variable, which affects the control performance. However, in practical applications, the total disturbance of the system is not measurable. Therefore, it is necessary to design an anti-disturbance observer to observe the variation of the disturbance $d(t)$ to obtain a good anti-disturbance performance with high accuracy.

4.2. Stability proof of the system with sliding mode speed controller based on ASMRL

Theorem 1. *For a continuous time system, if it is possible to construct a scalar function $V(x)$ with a continuous first-order partial derivative function for x, and $V(0) = 0$, and the following condition is satisfied for all non-zero states x in the state space:*

1. $V(x)$ is positive definite.

2. $\dot{V}(x) \triangleq dV(x)/dt$ is negative definite.

3. When $\|t\| \to \infty$, there is $V(t) \to \infty$.

Then the equilibrium state of the system origin $x = 0$ is large range of uniformly asymptotic stability [36].

Proof. To prove the stability of the system with a sliding mode controller based on the ASMRL, the Lyapunov stability theorem, i.e., Theorem 1, is chosen to expand the proof.

The Lyapunov function of the following form is constructed.

$$V = \frac{1}{2}s^2 \tag{30}$$

The derivative of V is

$$\begin{aligned} \dot{V} &= s\dot{s} \\ &= -s\left[\varepsilon|x|^a \tanh(\lambda s) + ks\left(\alpha_1|s|^{\mathrm{b}} + \frac{\alpha_2}{|s|^{\mathrm{b}}}\right)\right] \end{aligned} \tag{31}$$

where ε, k are all positive constants, the checkmark function $\alpha_1|s|^b + \frac{\alpha_2}{|s|^b}$ is also positive, and the hyperbolic tangent function $\tanh(\lambda s)$ and the sign function $sgn(s)$ are the same positive or negative, so that (31) satisfies

$$\dot{V} \le 0 \tag{32}$$

The reaching condition of the sliding mode control and the Lyapunov stability condition are guaranteed.

4.3. Design of the SMDO

In the control object model (25), the total perturbation $d(t)$ of the system cannot be measured in practical applications. In order to further improve the robustness of the sliding mode control, an SMDO is designed in this study. This observer can observe the motor speed and disturbance, and compensate the observed disturbance to the control input, thus improving the robustness of the system. Extending $d(t)$ as a system state variable, (25) is then extended to a system of the following form.

$$\begin{bmatrix} \dot{\omega}_m \\ \dot{d}(t) \end{bmatrix} = \begin{bmatrix} -\frac{B}{J} & -\frac{1}{J} \\ 0 & 0 \end{bmatrix}\begin{bmatrix} \omega_m \\ d(t) \end{bmatrix} + \begin{bmatrix} \frac{1}{J} \\ 0 \end{bmatrix} T_e \tag{33}$$

For the system (33) an SMDO of the following form is designed.

$$\begin{bmatrix} \dot{\hat{\omega}}_m \\ \dot{\hat{d}}(t) \end{bmatrix} = \begin{bmatrix} -\frac{B}{J} & -\frac{1}{J} \\ 0 & 0 \end{bmatrix}\begin{bmatrix} \hat{\omega}_m \\ \hat{d}(t) \end{bmatrix} + \begin{bmatrix} \frac{1}{J} \\ 0 \end{bmatrix} T_e + \begin{bmatrix} 1 \\ l \end{bmatrix} y(e_\omega) \tag{34}$$

where $y(e_\omega)$ is the sliding mode rate of the sliding mode observer error, $e_\omega = \omega_m - \widehat{\omega}_m$, and l is the observer gain.

$$\begin{cases} \dot{e}_\omega = -\frac{B}{J}e_\omega - \frac{1}{J}e_d - y(e_\omega) \\ \dot{e}_d = -ly(e_\omega) \end{cases} \tag{35}$$

where e_ω and e_d are the speed observation error and the disturbance observation error, respectively.

In the SMDO, the integral type sliding mode surface is chosen as follows.

$$s_\omega = e_\omega + c_\omega \int e_\omega dt \tag{36}$$

where the derivative of the sliding mode surface (36) is

$$\dot{s}_\omega = \dot{e}_\omega + c_\omega e_\omega \tag{37}$$

Next, the reaching law is selected as follows.

$$\dot{s}_\omega = -\varepsilon_\omega \mathrm{sgn}(s_\omega) \tag{38}$$

where ε_ω is the switching gain of the reaching law.

Considering $-\frac{1}{J}e_d$ as the disturbance term, the control law of the SMDO can be obtained according to Eqs. (35)–(38) as

$$y(e_\omega) = \left(c_\omega - \frac{B}{J}\right)e_\omega + \varepsilon_\omega \mathrm{sgn}(s_\omega) \tag{39}$$

With the above designed SMDO, the total disturbance $d(t)$ of the system can be estimated, and then the estimated total disturbance is compensated into the speed control input $u(t)$, and the compensated control input is rewritten as

$$\begin{aligned} u(t) = \frac{1}{b}\Big[&\dot{\omega}_{ref} + c\omega_m - \hat{d}(t) + ce \\ &+ \varepsilon|x|^a \tanh(\lambda s) + ks\left(\alpha_1|s|^{\mathrm{b}} + \frac{\alpha_2}{|s|^b}\right) \end{aligned} \tag{40}$$

4.4. Convergence proof for SMDO

Theorem 2. *For the observation error function $e(t)$ between the observer (34) and the observed system (33), if there exist undetermined parameters that make the error function satisfy when $t \to 0$, $e(t) \to 0$, then the observer is convergent [19].*

Proof. The convergence of the SMDO proposed in the previous subsection is in the first place proved. It can be deduced that the reaching law (38) and the sliding mode surface (37) can satisfy the Lyapunov stability condition $\dot{V} = s_\omega \dot{s}_\omega \le 0$, i.e., under the effect of the sliding mode control law (38), the system trajectory

will eventually reach the sliding mode surface, and then the following equation is satisfied.

$$\begin{cases} s_\omega = \dot{s}_\omega = 0 \\ e_\omega = \dot{e}_\omega = 0 \end{cases} \tag{41}$$

Substituting (41) into (35), the error function of SMDO can be written as:

$$\begin{cases} e_d = -Jy\,(e_\omega) \\ \dot{e}_d = -ly\,(e_\omega) \end{cases} \tag{42}$$

Solving the first-order derivative function (42) gives

$$e_d = c_d e^{\frac{l}{J}t} \tag{43}$$

where c_d is a constant. From Eq. (43), it is clear that for the error of the disturbance observer to converge to zero, the observer gain needs to satisfy $l < 0$, and l directly affects the convergence rate of the observer.

4.5. Stability proof of the system with the ASMC combined with SMDO

To verify the stability of the system under the ASMC combined with the SMDO, the Lyapunov stability theorem, i.e., Theorem 1, is chosen to expand the proof.

Proof. The following Lyapunov function is constructed.

$$V = \frac{1}{2}s^2 \tag{44}$$

Combining (25)–(28) and (40), it can be deduced that

$$\dot{s} = -\varepsilon|x|^a \tanh(\lambda s) - ks\left(\alpha_1|s|^b + \frac{\alpha_2}{|s|^b}\right) + \left(d(t) - \hat{d}(t)\right) \tag{45}$$

Further, the derivative of V is given by

$$\begin{aligned} \dot{V} &= s\dot{s} \\ &= -s\left[\varepsilon|x|^a \tanh(\lambda s) + ks\left(\alpha_1|s|^b + \frac{\alpha_2}{|s|^b}\right) + (d(t) - \hat{d}(t))\right] \end{aligned} \tag{46}$$

According to the proof of convergence of SMDO, we can get $e_d \to 0$, and $e_d = d(t) - \hat{d}(t)$, so $d(t) - \hat{d}(t) \to 0$. Therefore, (46) satisfies

$$\dot{V} \le 0 \tag{47}$$

The Lyapunov stability condition is satisfied.

5. Experimental results and discussion

In order to verify the effectiveness of the ASMC proposed in this study, the speed and current waveforms of PI, TSMC, reference reaching law sliding mode control (RSMC) in [31], ASMC and ASMC combined with the SMDO (ASMC+SMDO) control strategies are compared in this section under several operating conditions, such as motor startup, motor forward and reverse rotation, sudden load and parameter mismatch. The structure diagram of the PMSM servo system based on ASMC+SMDO is given in Fig. 7. The flow chart of the ASMC+SMDO control strategy is given in Fig. 9. The PMSM is controlled by the field-oriented control (FOC) method, and ASMC+SMDO is used as the speed controller, where SMDO observes the estimated total disturbance $d(t)$ of the system, and then compensates the estimated total disturbance to ASMC, and finally the reference current i_{qref} of the current loop is output by ASMC.

The 707 W PMSM driver platform is given in Fig. 8, where the corresponding technical parameters of the PMSM are shown in Table 1. The control algorithms involved in this study are implemented in digital signal processing (DSP) using a C program and the core component of the controller is DSP-TMS320F280049. The core components of the driver are a DRV8350 three-phase smart gate driver and a power MOSFET. Load torque is generated by a hysteresis brake. An absolute encoder is installed at the end of the motor shaft to measure the digital position to obtain the speed of the PMSM.

Table 1
PMSM parameters.

Symbol	Description	Value and unit
P	Rate power	707 W
R	Armature resistance	0.12 Ω
L_d	Inductance of d axis	0.2 mH
L_q	Inductance of q axis	0.2 mH
K_t	Torque coefficient	0.46 Nm/A
n_p	Number of pole pairs	10
J	Moment of inertia	221×10^{-5} Kg · m^2

Table 2
Parameter values of the five control strategies.

Control strategy	Parameter value
PI	$k_p = 0.12$, $k_i = 0.6$
TSMC	$\varepsilon = 0.5$, $c = 8$, $k = 20$
RSMC	$\varepsilon = 0.5$, $c = 8$, $k = 20$, $a = 0.5$, $b = 0.3$
ASMC	$\varepsilon = 0.5$, $\lambda = 1$, $c = 8$, $k = 20$, $a = 0.5$, $b = 0.3$, $\alpha_1 = 2$, $\alpha_2 = 0.1$
ASMC+SMDO	$\varepsilon = 0.5$, $\lambda = 1$, $c = 8$, $k = 20$, $a = 0.5$, $b = 0.3$, $\alpha_1 = 2$, $\alpha_2 = 0.1$, $\varepsilon_\omega = 0.5$, $c_\omega = 30$, $l = -0.005$

To ensure the validity of the comparison experiments, PI control with the same parameters was used for the current loop controller for all experiments. The relevant parameters of the five control strategies for the speed loop are listed in Table 2.

5.1. Motor startup experiment

The first experiment compares the motor starting effects under five control strategies: PI, TSMC, RSMC, ASMC, and ASMC+SMDO. Fig. 10 shows the speed waveforms of the motor startup experiment under the five control strategies. Fig. 13 shows the local zoom of the motor startup speed waveforms under the five control strategies, and the speed overshoot δ and response time t_s are marked in Fig. 13. The motor starts at 1 s with a reference speed of 120 r/min. From Fig. 13, it can be seen that the overshoot of PI and TSMC is 9.9 r/min and 8.4 r/min, respectively. However, RSMC, ASMC, and ASMC+SMDO almost have no overshoot. The response times of PI, TSMC, RSMC, ASMC, and ASMC+SMDO are 0.85 s, 0.77 s, 0.095 s, 0.069 s, and 0.043 s, respectively.

Fig. 11 shows the q-axis current waveforms for the motor startup experiments under the five control strategies. The local zoom in Fig. 11 shows that the q-axis currents under ASMC and ASMC+SMDO control strategies are able to converge to a steady state more quickly.

Fig. 12 gives the histograms of the experimental performance comparison of the motor startup, and the speed overshoot and response time are selected as the comparison terms. As shown in Fig. 12, PI overshoot is larger than TSMC, while RSMC, ASMC, and ASMC+SMDO have almost no overshoot. The response time from slow to fast is PI, TSMC, RSMC, ASMC, ASMC+SMDO. In the overall comparison, ASMC+SMDO has the best performance with the fastest response time and no overshoot.

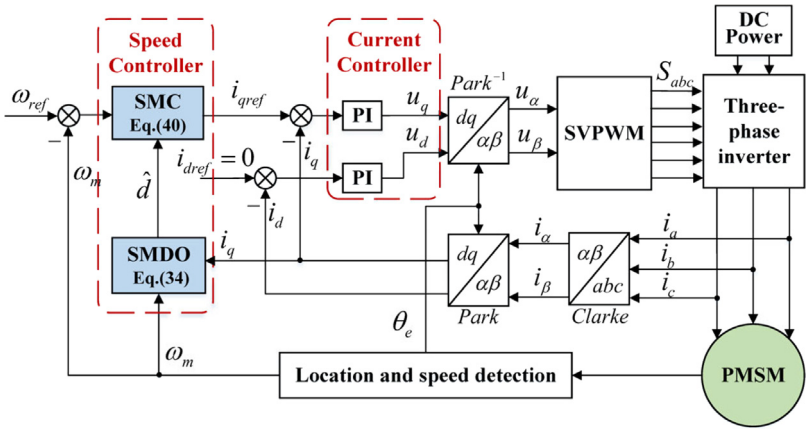

Fig. 7. Structure diagram of PMSM servo system based on ASMC+SMDO.

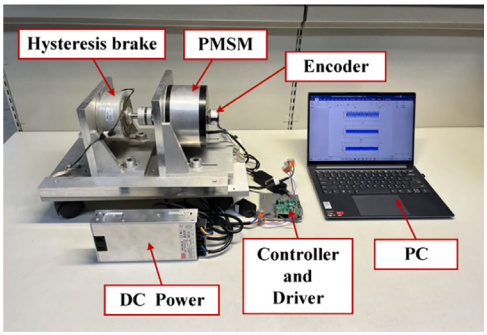

Fig. 8. Photograph of the experimental platform.

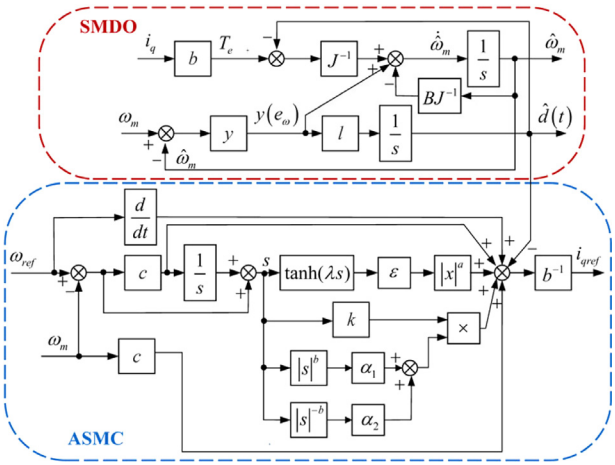

Fig. 9. Flow chart of ASMC+SMDO control strategy.

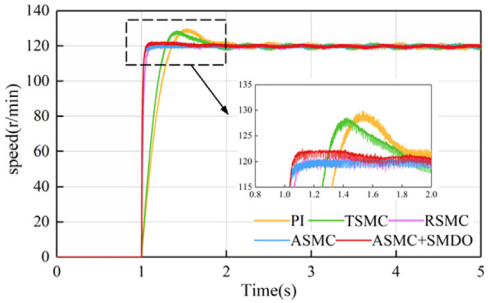

Fig. 10. Speed waveforms of motor startup.

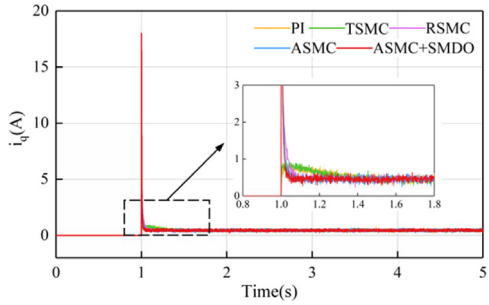

Fig. 11. q-axis current waveforms of motor start.

5.2. Motor forward and reverse rotation experiment

The second experiment compares the experimental effect of motor forward and reverse rotation under the PI, TSMC, RSMC, ASMC, and ASMC+SMDO control strategies. Fig. 14 shows the speed waveforms of the motor forward and reverse rotation under the five control strategies. The two local zooms of Fig. 14 show that PI and TSMC have obvious speed overshoot and long response time. The speed waveforms of RSMC, ASMC, and ASMC+SMDO control strategies can keep up with the reference speed well. The performance of ASMC+SMDO is better than ASMC, and ASMC is better than RSMC.

Fig. 15 shows the q-axis current waveforms of the motor in forward and reverse rotation for the five control strategies. From the two local zooms of Fig. 15, it can be seen that ASMC and ASMC+SMDO can make the q-axis current converge to a steady state more quickly than the other three control strategies.

In summary, among the five control strategies, PI and TSMC have poor effects, and RSMC, ASMC, ASMC+SMDO have better performance in the motor forward and reverse experiments. And with reference to the speed and current waveforms, ASMC+SMDO has better performance than ASMC and ASMC has better performance than RSMC.

5.3. Load torque experiment

The third experiment is the comparison of experimental effects of sudden load torque under the PI, TSMC, RSMC, ASMC, and ASMC+SMDO control strategies. The speed waveforms and the q-axis current waveforms of the five control strategies are shown in Fig. 16 and Fig. 17, respectively, for a sudden load of 0.8 N · m at a speed of 120 r/min. Fig. 18 gives a performance comparison histogram of the load torque experiment for the five control

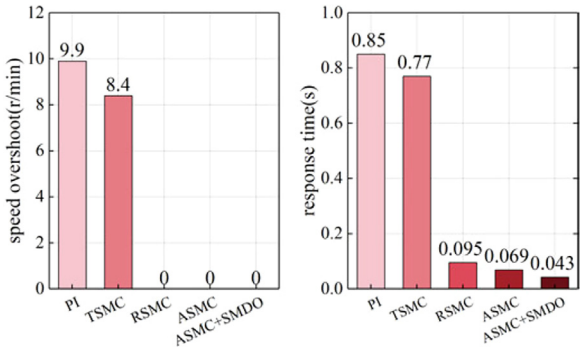

Fig. 12. Performance comparison of motor startup experiments.

strategies. As shown in Fig. 18, the maximum speed drop of PI, TSMC, RSMC, ASMC, and ASMC+SMDO are 97.6 r/min, 83.2 r/min, 14.0 r/min, 8.6 r/min, 7.4 r/min, respectively. The adjustment times are 1.08 s, 1.07 s, 0.69 s, 0.62 s, 0.37 s, respectively.

Comprehensive analysis shows that the maximum speed drop value of PI, TSMC, RSMC, ASMC, ASMC+SMDO decreases successively and the adjustment time also decreases successively. In other words, the proposed ASMRL has better anti-disturbance performance, and ASMC+SMDO has the best anti-disturbance performance.

5.4. Parameter mismatch experiment

The fourth experiment is the parameter mismatch experiment under the PI, TSMC, RSMC, ASMC, and ASMC+SMDO control strategies. The experiments were done with the inertia J mismatching to half of the calibration value and double the calibration value, respectively. Fig. 19 and Fig. 20 show the speed waveforms and q-axis current waveforms when the inertia J is suddenly mismatched to half of the calibration value ($0.5J$) at 2 s, respectively. Among them, the speed maximum ω_{max}, speed minimum ω_{min}, maximum speed fluctuation $\Delta\omega$ and the standard deviation σ at 4 s–5 s steady state are given in Table 3. Considering Fig. 19 and Table 3 together, it can be seen that the maximum speed fluctuation values of TSMC, RSMC, ASMC, and ASMC+SMDO are 36.3 r/min, 11.1 r/min, 7.7 r/min, and 4.2 r/min with the parameter J mismatch to $0.5J$. Among them, TSMC, RSMC, and ASMC all have obvious speed drop phenomenon. It is worth noting that under the ASMC+SMDO strategy, the speed almost did not drop suddenly. After the speed drop, all four control strategies converge the speed to the reference speed. After speed stability, the standard deviations of TSMC, RSMC, ASMC, and ASMC+SMDO at 4 s–5 s are 0.9479 r/min, 0.5067 r/min, 0.4624 r/min, and 0.8042 r/min, respectively. Compared to TSMC, the steady state performance of RSMC, ASMC, and ASMC+SMDO after parameter mismatch has been improved in different degrees.

The local zoom in Fig. 20 shows that the q-axis currents under the control of TSMC, RSMC, and ASMC have different degrees of decrease in the case of sudden parameter mismatch. Among them, TSMC decreases more than RSMC, RSMC decreases more than ASMC, and the larger the current decrease, the longer the time to recover the steady state. And under the control of ASMC+SMDO, the q-axis current has no significant mutation.

Figs. 21 and 22 show the speed waveforms and q-axis current waveforms when the inertia J is suddenly mismatched to double calibration value ($2J$) at 2 s, respectively. Among them, the speed maximum ω_{max}, speed minimum ω_{min}, maximum speed fluctuation $\Delta\omega$ and the standard deviation σ at 4 s–5 s steady state are given in Table 4 . Considering Fig. 21 and Table 4 together, it can be seen that the maximum speed fluctuation values of TSMC, RSMC, and ASMC are 24.4 r/min, 8.5 r/min, 6.5 r/min and 2.9 r/min, respectively. Among them, TSMC, RSMC, and ASMC all showed significant speed rise. Similarly, there is almost no sudden speed rise under the ASMC+SMDO strategy. After the speed drop, all four control strategies converge the speed to the reference speed. After speed stability, the standard deviations of TSMC, RSMC, ASMC, and ASMC+SMDO at 4 s–5 s are 0.5861 r/min, 0.4301 r/min, 0.4383 r/min, and 0.4483 r/min, respectively. Compared to TSMC, the steady-state performance of RSMC, ASMC, and ASMC+SMDO after parameter mismatch has been improved in different degrees.

Table 3
Performance comparison of parameter mismatch experiment ($0.5J$).

Control strategy	ω_{max} (r/min)	ω_{min} (r/min)	$\Delta\omega$ (r/min)	σ (r/min)
TSMC	125.7	89.4	36.3	0.9479
RSMC	121.0	109.9	11.1	0.5067
ASMC	120.8	113.1	7.7	0.4624
ASMC+SMDO	121.8	117.6	4.2	0.8042

Table 4
Performance comparison of parameter mismatch experiment ($2J$).

Control strategy	ω_{max} (r/min)	ω_{min} (r/min)	$\Delta\omega$ (r/min)	σ (r/min)
TSMC	142.0	117.6	24.4	0.5861
RSMC	126.7	118.2	8.5	0.4301
ASMC	124.6	118.1	6.5	0.4383
ASMC+SMDO	121.1	118.2	2.9	0.4483

It can be observed from the local zoom of the currents in Fig. 22 that the q-axis currents under the control strategy of TSMC, RSMC, and ASMC have different degrees of rising in the case of sudden parameter mismatch. Among them, the rising value of TSMC is larger than RSMC, and RSMC is larger than TSMC, and the larger the rising value of current, the longer it takes to recover the steady state. However, under the control of ASMC+SMDO, there is no significant mutation of the q-axis current.

In summary, the speed fluctuations and current fluctuations of the two groups of parameter mismatch experiments show that the control strategies affected by parameter mismatch are TSMC, RSMC, ASMC, and ASMC+SMDO in descending order. However, after returning to the steady state, the steady state performance under RSMC, ASMC, and ASMC+SMDO control strategies are improved in different degrees compared to TSMC. In other words, the ASMC control strategy has better dynamic characteristics under the same parameter mismatch. And the ability to resist parameter mismatch is better by adding SMDO based on ASMC.

6. Conclusion

In this paper, an ASMRL is proposed based on the TSMRL, a sliding mode controller is designed based on the ASMRL. Then SMDO is designed to observe the total disturbance of the system, and the estimated total disturbance is compensated to ASMC to improve the anti-disturbance performance of the system. The stabilities of the system applying ASMC, ASMC+SMDO control strategies are proved by Lyapunov's stability theorem. The ASMRL has a faster convergence speed and smaller chattering. The performance of several control strategies, including PI, TSMC, RSMC, ASMC, and ASMC+SMDO, are compared on the PMSM experimental platform. The experimental results show that ASMC has better performance than PI, TSMC, RSMC under the conditions of motor startup, motor forward and reverse rotation, sudden load disturbance, and parameter mismatch, and the performance of ASMC combined with SMDO is better after compensating the disturbance.

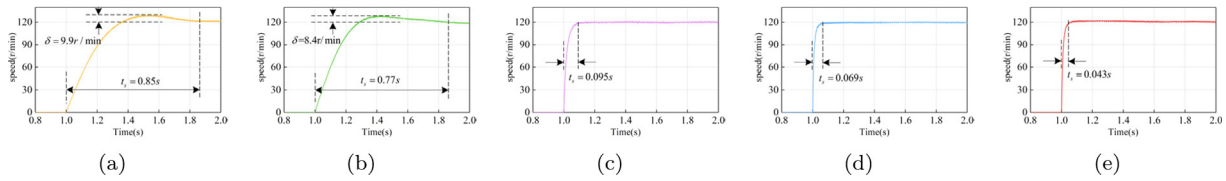

Fig. 13. Local zoom of motor startup speed waveforms. (a) PI (b) TSMC (c) RSMC (d) ASMC (e) ASMC+SMDO.

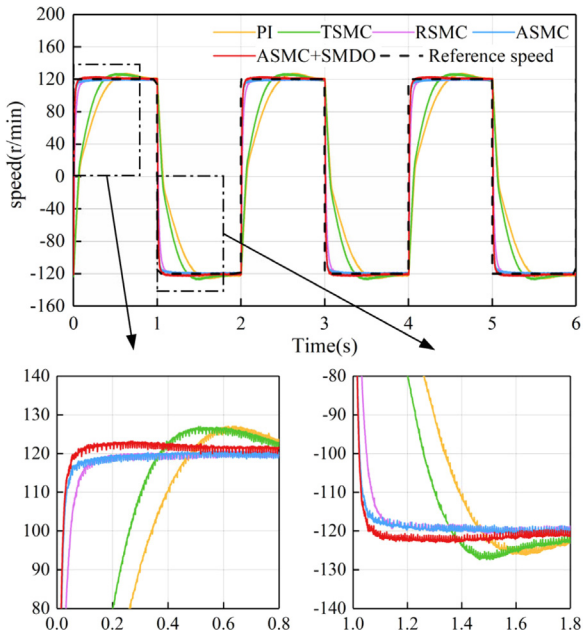

Fig. 14. Speed waveforms of motor forward and reverse rotation experiment.

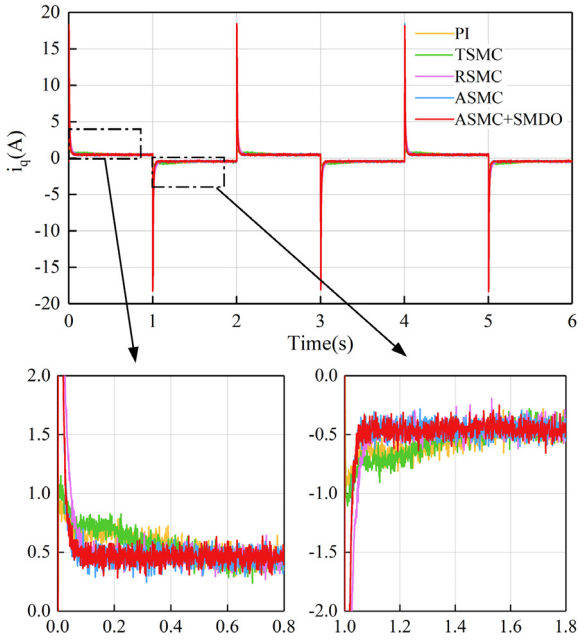

Fig. 15. *q*-axis current waveforms of motor forward and reverse experiment.

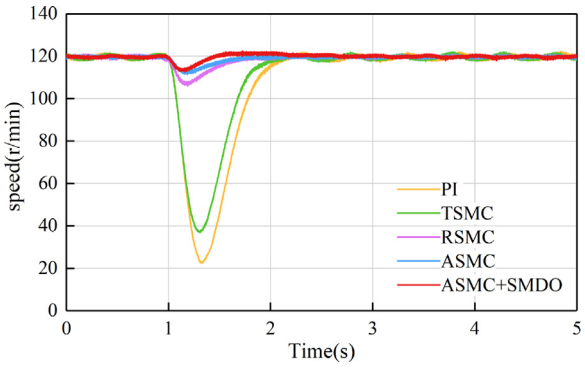

Fig. 16. Speed waveforms of load torque experiment.

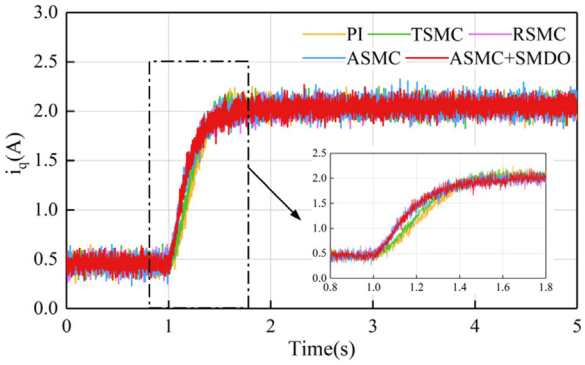

Fig. 17. *q*-axis current waveforms of load torque experiment.

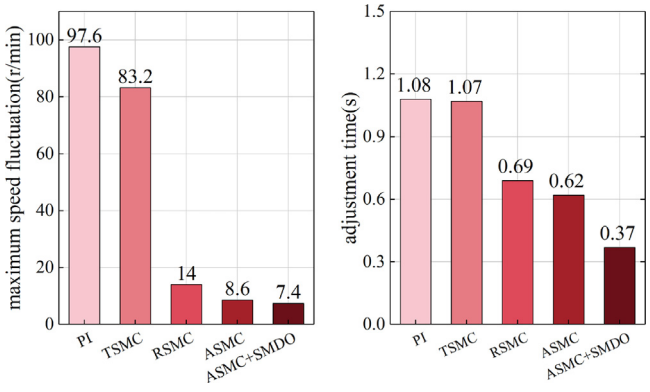

Fig. 18. Performance comparison of five control strategies under 0.8 N·m sudden load.

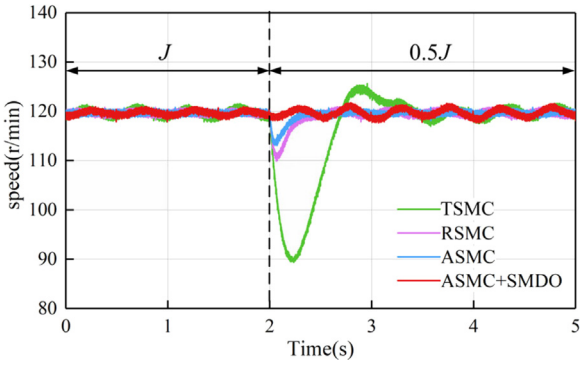

Fig. 19. Speed waveforms under parameter mismatch of 0.5*J*.

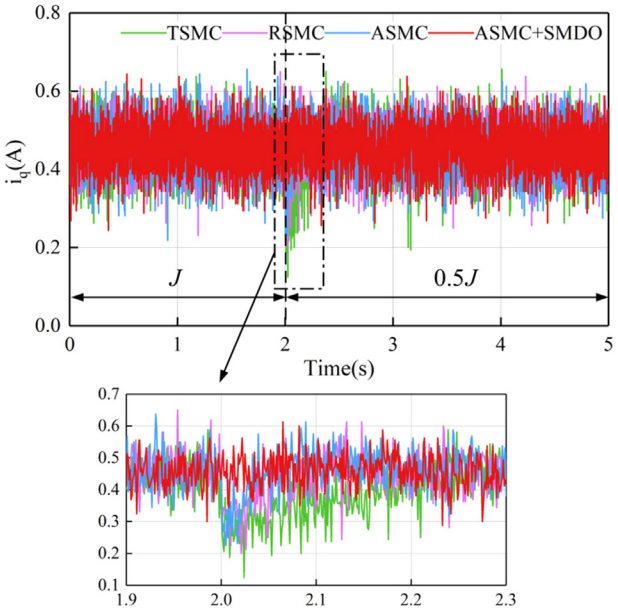

Fig. 20. Current waveforms of *q*-axis under parameter mismatch of 0.5*J*.

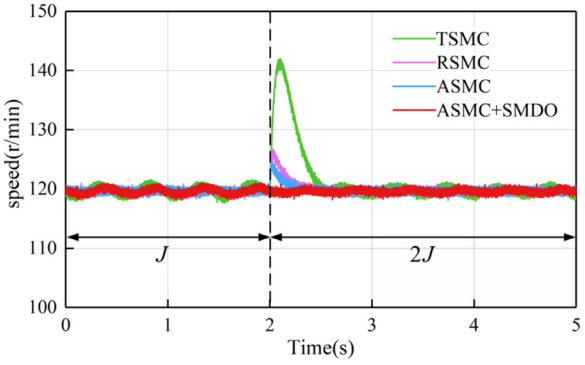

Fig. 21. Speed waveforms under parameter mismatch of 2*J*.

Declaration of competing interest

The authors declare that they have no known competing financial interests or personal relationships that could have appeared to influence the work reported in this paper.

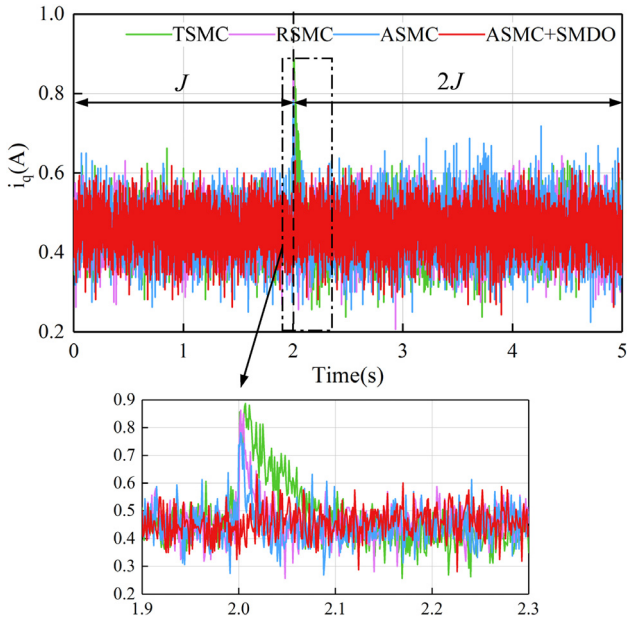

Fig. 22. Current waveforms of *q*-axis under parameter mismatch of 2*J*.

Acknowledgment

This work was supported by the Scientific research business fee fund of Heilongjiang provincial scientific research institutes under Grant CZKYF2020B009.

References

[1] Deng Y, Wang J, Li H, Liu J, Tian D. Adaptive sliding mode current control with sliding mode disturbance observer for PMSM drives. ISA Trans 2019;88:113–26. http://dx.doi.org/10.1016/j.isatra.2018.11.039, 1.

[2] Jung J-W, Leu VQ, Do TD, Kim E-K, Choi HH. Adaptive PID speed control design for permanent magnet synchronous motor drives. IEEE Trans Power Electron 2015;30(2):900–8. http://dx.doi.org/10.1109/TPEL.2014.2311462, 2.

[3] Guo B, Bacha S, Alamir M. A review on ADRC based PMSM control designs. In: IECON 2017 - 43rd annual conference of the IEEE industrial electronics society. 2017, p. 1747–53. http://dx.doi.org/10.1109/IECON.2017.8216296, 3.

[4] Qu L, Qiao W, Qu L. An extended-state-observer-based sliding-mode speed control for permanent-magnet synchronous motors. IEEE J Emerg Sel Top Power Electron 2021;9(2):1605–13. http://dx.doi.org/10.1109/JESTPE.2020.2990442, 4.

[5] Qu Z, Du Z, Kao Y, Wu Z. Fuzzy event-triggered tracking control for nonlinear unreliable networked systems. ISA Trans 2022. http://dx.doi.org/10.1016/j.isatra.2022.07.011, S0019057822003676.

[6] Xu S, Wen H, Wang X. Observer-based robust fuzzy control of nonlinear networked systems with actuator saturation. ISA Trans 2022;123:122–35. http://dx.doi.org/10.1016/j.isatra.2021.05.037, 6.

[7] Wang H, Chen X, Liu Y, Su M, Feng W, Yu W. Model predictive control of three-phase voltage-source converters with improved tracking performance. ISA Trans 2022. http://dx.doi.org/10.1016/j.isatra.2022.07.012, S0019057822003664, 7.

[8] Zhang Y, Wang X, Yang H, Zhang B, Rodriguez J. Robust predictive current control of induction motors based on linear extended state observer. Chin J Electr Eng 2021;7(1):94–105. http://dx.doi.org/10.23919/CJEE.2021.000009, 8.

[9] Li J, Xia Y, Qi X, Gao Z. On the necessity, scheme, and basis of the linear–Nonlinear switching in active disturbance rejection control. IEEE Trans Ind Electron 2017;64(2):1425–35. http://dx.doi.org/10.1109/TIE.2016.2611573, 9.

[10] Lin P, Wu Z, Liu K-Z, Sun X-M. A class of linear–Nonlinear switching active disturbance rejection speed and current controllers for PMSM. IEEE Trans Power Electron 2021;36(12):14366–82. http://dx.doi.org/10.1109/TPEL.2021.3086273, 10.

[11] Liu W, Zhao T. An active disturbance rejection control for hysteresis compensation based on Neural Networks adaptive control. ISA Trans 2021;109:81–8. http://dx.doi.org/10.1016/j.isatra.2020.10.019, 11.

[12] Patan K, Patan M. Neural-network-based iterative learning control of nonlinear systems. ISA Trans 2020;98:445–53. http://dx.doi.org/10.1016/j.isatra.2019.08.044, 12.
[13] Kang E, Qiao H, Gao J, Yang W. Neural network-based model predictive tracking control of an uncertain robotic manipulator with input constraints. ISA Trans 2021;109:89–101. http://dx.doi.org/10.1016/j.isatra.2020.10.009, 13.
[14] Zheng W, Chen Y, Wang X, Chen Y, Lin M. Enhanced fractional order sliding mode control for a class of fractional order uncertain systems with multiple mismatched disturbances. ISA Trans 2022. http://dx.doi.org/10.1016/j.isatra.2022.07.002, S0019057822003585, 14.
[15] Shen G, Xia Y, Zhang J, Cui B. Adaptive super-twisting sliding mode altitude trajectory tracking control for reentry vehicle. ISA Trans 2022. http://dx.doi.org/10.1016/j.isatra.2022.06.023, S0019057822003317, 15.
[16] Sun G, Ma Z, Yu J. Discrete-time fractional order terminal sliding mode tracking control for linear motor. IEEE Trans Ind Electron 2018;65(4):3386–94. http://dx.doi.org/10.1109/TIE.2017.2748045, 16.
[17] Zaihidee FM, Mekhilef S, Mubin M. Application of fractional order sliding mode control for speed control of permanent magnet synchronous motor. IEEE Access 2019;7:101765–74. http://dx.doi.org/10.1109/ACCESS.2019.2931324, 17.
[18] Levant A. Chattering analysis. IEEE Trans Automat Control 2010;55(6):1380–9. http://dx.doi.org/10.1109/TAC.2010.2041973.
[19] Wang Y, Feng Y, Zhang X, Liang J, Cheng X. New reaching law control for permanent magnet synchronous motor with extended disturbance observer. IEEE Access 2019;7:186296–307. http://dx.doi.org/10.1109/ACCESS.2019.2956846, 18.
[20] Chandra A, Lal PP. Higher order sliding mode controller for a quadrotor UAV with a suspended load. IFAC-PapersOnLine 2022;55(1):610–5. http://dx.doi.org/10.1016/j.ifacol.2022.04.100, 19.
[21] Zhang L, Nan H, Zhao Z, Yuan Y. Adaptive disturbance observer-based dual-loop integral-type fast terminal sliding mode control for micro spacecraft and its gimbal tracking device. ISA Trans 2022. http://dx.doi.org/10.1016/j.isatra.2022.03.010, S0019057822001306, 20.
[22] Meng C-c, Zhang X-y. Distributed leaderless formation control for multiple autonomous underwater vehicles based on adaptive nonsingular terminal sliding mode. Appl Ocean Res 2021;115:102781. http://dx.doi.org/10.1016/j.apor.2021.102781, 21.
[23] Sami I, Ullah S, Ullah N, Ro J-S. Sensorless fractional order composite sliding mode control design for wind generation system. ISA Trans 2021;111:275–89. http://dx.doi.org/10.1016/j.isatra.2020.11.001, 22.
[24] Fei J, Lu C. Adaptive sliding mode control of dynamic systems using double loop recurrent neural network structure. IEEE Trans Neural Netw Learn Syst 2018;29(4):1275–86. http://dx.doi.org/10.1109/TNNLS.2017.2672998, 23.
[25] Guo X, Yin Z, Zhang Y, Bai C. Position sensorless control of PMLSM based on adaptive complex coefficient sliding mode observer. Energy Rep 2022;8:687–95. http://dx.doi.org/10.1016/j.egyr.2022.02.271.
[26] Wang G, Zhang H. A new speed adaptive estimation method based on an improved flux sliding-mode observer for the sensorless control of PMSM drives. ISA Trans 2021. http://dx.doi.org/10.1016/j.isatra.2021.09.003, S0019057821004870, 25.
[27] Yan X-G, Spurgeon SK, Edwards C. State and parameter estimation for nonlinear delay systems using sliding mode techniques. IEEE Trans Automat Control 2013;58(4):1023–9. http://dx.doi.org/10.1109/TAC.2012.2215531.
[28] Sun X, Cao J, Lei G, Guo Y, Zhu J. A composite sliding mode control for SPMSM drives based on a new hybrid reaching law with disturbance compensation. IEEE Trans Transp Electr 2021;7(3):1427–36. http://dx.doi.org/10.1109/TTE.2021.3052986, 26.
[29] Mozayan SM, Saad M, Vahedi H, Fortin-Blanchette H, Soltani M. Sliding Mode Control of PMSG Wind Turbine Based on Enhanced Exponential Reaching Law. IEEE Trans Ind Electron 2016;63(10):6148–59. http://dx.doi.org/10.1109/TIE.2016.2570718.
[30] Leśniewski P, Bartoszewicz A. Non-switching reaching law based discrete time quasi-sliding mode control with application to warehouse management problem. IFAC Proc Vol 2014;47(3):4589–94. http://dx.doi.org/10.3182/20140824-6-ZA-1003.00181.
[31] Wang Y, Feng Y, Zhang X, Liang J. A New Reaching Law for Antidisturbance Sliding-Mode Control of PMSM Speed Regulation System. IEEE Trans Power Electron 2020;35(4):4117–26. http://dx.doi.org/10.1109/TPEL.2019.2933613, 27.
[32] Junejo AK, Xu W, Mu C, Ismail MM, Liu Y. Adaptive Speed Control of PMSM Drive System Based a New Sliding-Mode Reaching Law. IEEE Trans Power Electron 2020;35(11):12110–21. http://dx.doi.org/10.1109/TPEL.2020.2986893, 28.
[33] Krishnan R. Permanent magnet synchronous and brushless DC motor drives. Boca Raton: CRC Press/Taylor & Francis; 2010, 29.
[34] Qu S, Xu W, Zhao J, Zhang H. Design and implementation of a fast sliding-mode speed controller with disturbance compensation for SPMSM system. IEEE Trans Transp Electr 2021;7(4):2611–22. http://dx.doi.org/10.1109/TTE.2021.3060102, 30.
[35] Gao W, Hung J. Variable structure control of nonlinear systems: A new approach. IEEE Trans Ind Electron 1993;40(1):45–55. http://dx.doi.org/10.1109/41.184820.
[36] Zheng D. Linear system theory. 2nd ed. Beijing, China: Tsinghua University Press; 2002.